Monthly Notices
of the
ROYAL ASTRONOMICAL SOCIETY

MNRAS **502,** 176–187 (2021) doi:10.1093/mnras/staa3573

‘Ears’ formation in supernova remnants: overhearing an interaction history with bipolar circumstellar structures

A. Chiotellis,* P. Boumis and Z. T. Spetsieri

Institute for Astronomy, Astrophysics, Space Applications and Remote Sensing, National Observatory of Athens, 15236, Penteli, Greece

Accepted 2020 November 10. Received 2020 November 8; in original form 2020 October 29

ABSTRACT

A characteristic feature that is frequently found in nearby supernova remnants (SNRs) is the existence of two antisymmetric, local protrusions that are projected as two ‘ears’ in the morphology of the nebula. In this paper, we present a novel scenario for the ‘ear’ formation process, according to which the two lobes are formed through the interaction of the SNR with a bipolar circumstellar medium (CSM) that was surrounding the explosion’s centre. We conduct two-dimensional hydrodynamic simulations and we show that the SNR shock breakout from the bipolar CSM triggers the inflation of two opposite protrusions at the equator of the remnant, which retain their size and shape from several hundreds up to a few thousand years of the SNR evolution. We run a set of models by varying the supernova (SN) and CSM properties and we demonstrate that the extracted results reveal good agreement with the observables, regarding the sizes, lifespan, morphology and kinematics of the ‘ears’. We discuss the plausibility of our model in nature and we suggest that the most likely progenitors of the ‘ear-carrying’ SNRs are the luminous blue variables or the red/yellow supergiants for the SNRs resulting from core collapse SN events, and the symbiotic binaries or the planetary nebulae for the SNRs formed by Type Ia SNe. Finally, we compare our model with other ‘ear’ formation models found in the literature and we show that there are distinctive differences among them, concerning the orientation of the ‘ears’ and the phase in which the ‘ear’ formation process occurs.

Key words: hydrodynamics – ISM: individual objects: Kepler’s SNR – ISM: individual objects: G1.9+0.3 – ISM: individual objects: G309.2–06 – ISM: jets and outflows – ISM: supernova remnants.

1 INTRODUCTION

Supernova remnants (SNRs) are the aftermath of supernova (SN) explosions that result from the interaction of the supersonically moving stellar ejecta with the ambient medium. These celestial nebulae reveal complex morphological properties in several spatial scales and all over the electromagnetic spectrum. There is a consensus that the complex properties of SNRs are mainly determined by two parameters: the nature of the parent’s stellar explosion, and the interaction of the SN ejecta with circumstellar structures sculptured by the mass outflows of their progenitor stellar systems. Thus, the peculiar morphological features of SNRs (e.g. asymmetries, inhomogeneities, hydrodynamic instabilities, rings, bow shocks and jets) host crucial encoded information about the mechanism of SN explosions and the nature and evolution of their stellar progenitors. In order to decipher this information and to meticulously separate the ‘cause and effect’ that lead to the observed properties of detailed modelling is required (e.g. Dwarkadas & Chevalier 1998; Ellison, Decourchelle & Ballet 2004; Badenes et al. 2006; Chiotellis, Schure & Vink 2012; Warren & Blondin 2013; Orlando et al. 2020).

A morphological peculiarity that is frequently found in SNRs is the presence of two antisymmetric protrusions at the outermost region of the remnant. These protrusions, which are frequently called ‘ears’, penetrate and deform the forward shock of the SNRs, thus shaping two opposite, local lobes in the overall morphology of the remnant. These ‘ears’ have been observed in all types of SNRs (Type Ia and core collapse) and all evolutionary stages (from young X-ray bright remnants to well-evolved non-adiabatic SNRs). Characteristic cases are the Galactic SNRs of Kepler’s SNR (SN 1604), G1.9+0.3, G309.2–06 and S147 (see Fig. 1); see also Bear, Grichener & Soker (2017) and Tsebrenko & Soker (2015a) for a complete list of SNRs that possess antisymmetric ‘ear-like’ features. A common characteristic for all cases is the remarkable symmetry of the ‘ears’ in terms of brightness and shape, as well as their opposed positions with respect to the centre of the remnant. These properties advocate an axis or central symmetric formation mechanism more relevant to the nature of their parent stellar progenitor and/or SN explosion than local interstellar medium (ISM) inhomogeneities.

To date, the formation of the ‘ears’ in SNRs has been attributed to the launch of two opposite jets that accompany the SN explosion, or are triggered after it, which protrude the forward shock of the SNR and inflate the two opposite lobes (Gaensler, Green & Manchester 1998; Castelletti et al. 2006; Tsebrenko & Soker 2013; Bear et al. 2017; Grichener & Soker 2017; Yu & Fang 2018; Millas, Porth & Keppens 2019). For the case of SNRs that result from Type Ia SNe (SNe Ia), it has also been suggested that the ‘ears’ pre-existed in the morphology of a planetary nebula (PN) that surrounded the explosion’s centre (Tsebrenko & Soker 2013, 2015b). In this scenario, the ‘ears’ of the SNR were sculptured by the interaction

* E-mail: a.chiotellis@noa.gr

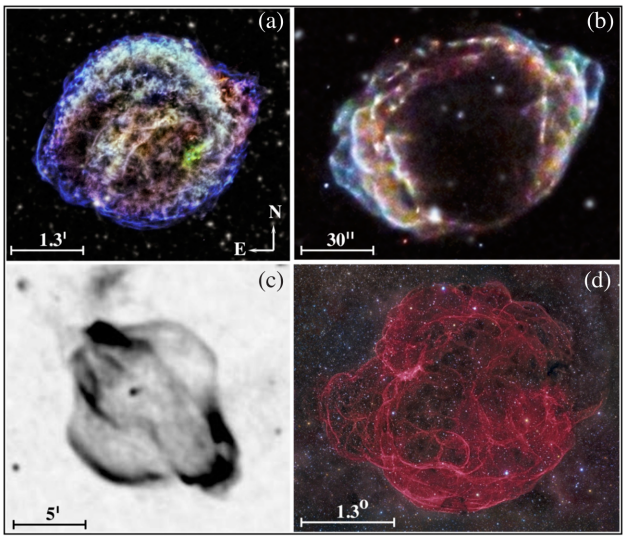

Figure 1. Characteristic cases of SNRs that reveal two antisymmetric 'ears' in their morphology: (a) an X-ray image of Kepler's SNR (SN 1604; Reynolds et al. 2007); (b) an X-ray image of the young SNR G1.9+0.3 (Borkowski et al. 2013); (c) a radio image of G309.2–06 at 1.3 GHz (Gaensler et al. 1998); (d) an H_α image mosaic of S147 (Drew et al. 2005). North (N) is to the top and east (E) is to the left in all images, as shown in (a).

of the SN ejecta with the shell of the surrounding 'ear-carrying' PN. Finally, Tsebrenko & Soker (2015c) suggested that the 'ears' of SNRs resulting from SNe Ia are shaped by iron clumps, or 'bullets', in the dense ejecta, formed along a common axis because of the rotation of the white dwarf progenitor. See also Soker (2019) for a thorough discussion of the evidence and constraints imposed by the 'ears' in SNRs regarding their parent SN Ia explosion.

Blondin, Lundqvist & Chevalier (1996) suggested an alternative scenario for the formation of the SNR's protrusions, according to which the two 'ears' are inflated during the evolution of the remnant within an axisymmetric circumstellar structure characterized by a high-density enhancement at the equatorial plane. They considered a circumstellar medium (CSM) described by a wind bubble in which the density is a function of the polar angle and increases from the poles to the equator of the system. Performing hydrodynamic simulations, they showed that the interaction of the SN ejecta with such an axisymmetric ambient medium results in the appearance of two protrusions close to the polar axis of the remnant. Depending on the polar density gradient, this can be extended at a length up to two to four times the overall radius of the remnant.

In this paper, we propose a novel mechanism for the formation of 'ears' in SNRs. We retain the idea of Blondin et al. (1996) regarding the SNR interaction with a bipolar and equatorially confined circumstellar structure, but we examine the 'ear' formation process under a different aspect. We state that the two opposite protrusions observed in several SNRs are formed at the equatorial plane of the remnant during the forward shock's breakout from the surrounding bipolar CSM. These protrusions maintain their shape from hundreds up to a few thousand years after the shock breakout, giving the impression of two 'ears' in the overall morphology of the SNR. In other words, we claim that the SNRs that host two opposite lobes had an interaction history with a dense and equatorially confined CSM, and that they are currently evolving in a less dense ambient medium. Using hydrodynamic simulations, we demonstrate that this model can account for the morphological and kinematic properties of the antisymmetric protrusions observed in several SNRs.

The paper is organized as follows. In Section 2, we describe our numerical model for the interaction between the SNR and the bipolar CSM, and we present the results of our hydrodynamic simulations. Moreover, we emphasize the mechanism of 'ear' formation and we articulate the dependence of our model's results on the properties of the CSM and the SN explosion. In Section 3, we compare the results extracted by our model to the relevant observable, we discuss the plausibility of our model in nature and, also, we present the differences between our model and other models of 'ear' formation presented in the literature. Finally, in Section 4, we summarize our main results and conclusions.

2 HYDRODYNAMIC MODELLING

The simulations of the bipolar CSM formation and the subsequent interaction of the SNR with it are performed using the hydrodynamic code AMRVAC (Keppens et al. 2003). We employ a two-dimensional (2D) grid in spherical coordinates and assume symmetry in the third dimension of the azimuthal angle. The radial span R of the computational domain is 18 pc while the polar angle θ ranges from 0° to 180°. Our grid consists of $(R \times \theta) = 360 \times 120$ grid cells. We exploit the adaptive mesh capabilities of the AMRVAC code by using four refinement levels of resolution, at each of which the resolution is doubled as a result of large gradients in density and/or energy. Hence, the maximum effective resolution becomes 6.25×10^{-3} pc by $0.^\circ19$. Radiative cooling is prescribed using the cooling curve of Schure et al. (2009).

2.1 Formation of the bipolar CSM

We first simulate the formation of the bipolar circumstellar structure. Considering that the mass-losing progenitor star/system is located at the axis origin of our grid, the CSM bubble is created by injecting material into the computational domain through the cells at the inner radial boundary. This inflow is in the form of a slow, continuous and equatorially focused stellar wind. Assuming that the stellar wind is axisymmetric in the azimuthal dimension, we describe the properties of the bipolar wind with the following trigonometrical functions:

$$u_{\rm w}(\theta) = u_{\rm w,p}\left[1 - \alpha|\sin\theta|^k\right]; \quad (1)$$

$$\rho(\theta) = \frac{\dot{M}_{\rm p}[1 - \beta|\sin\theta|^k]^{-1}}{4\pi r^2 u_{\rm w}(\theta)}. \quad (2)$$

Here, $\rho(\theta)$ and $u_{\rm w}(\theta)$ are the wind density profile and terminal velocity at the polar angle θ, respectively, $u_{\rm w,p}$ is the terminal velocity and $\dot{M}_{\rm p}$ is the mass-loss rate of the stellar wind at the poles of the system ($\theta = 0^\circ$). In equation (2), the symbol r refers to the radial distance from the mass-losing star. Note that α, β and k are constants that determine the polar distribution of the CSM density and velocity from the poles to the equatorial plane. Specifically, α and β ($0 \leq \alpha, \beta < 1$) stand for the ratio of the polar and equatorial velocity and density, respectively, where for a given r we obtain $\rho_{\rm eq}/\rho_{\rm p} = [(1-\alpha)(1-\beta)]^{-1}$ and $u_{\rm w,eq}/u_{\rm w,p} = (1-\alpha)$. Finally, the index $k > 0$ determines the angular density gradient and the confinement level of the stellar wind at the equatorial plane. For small values of k, the CSM density and velocity gradually change (increase and decrease, respectively) from poles to equator, while for $k \gg 1$ a disc-like morphology is shaped, confined in the equatorial plane that is surrounded by a roughly spherical wind bubble (see Figs 2a and b).

The polar distribution of the CSM density and radial velocity has a direct impact on the radius of the wind bubble at each polar angle, which in turn determines the overall shape of the circumstellar

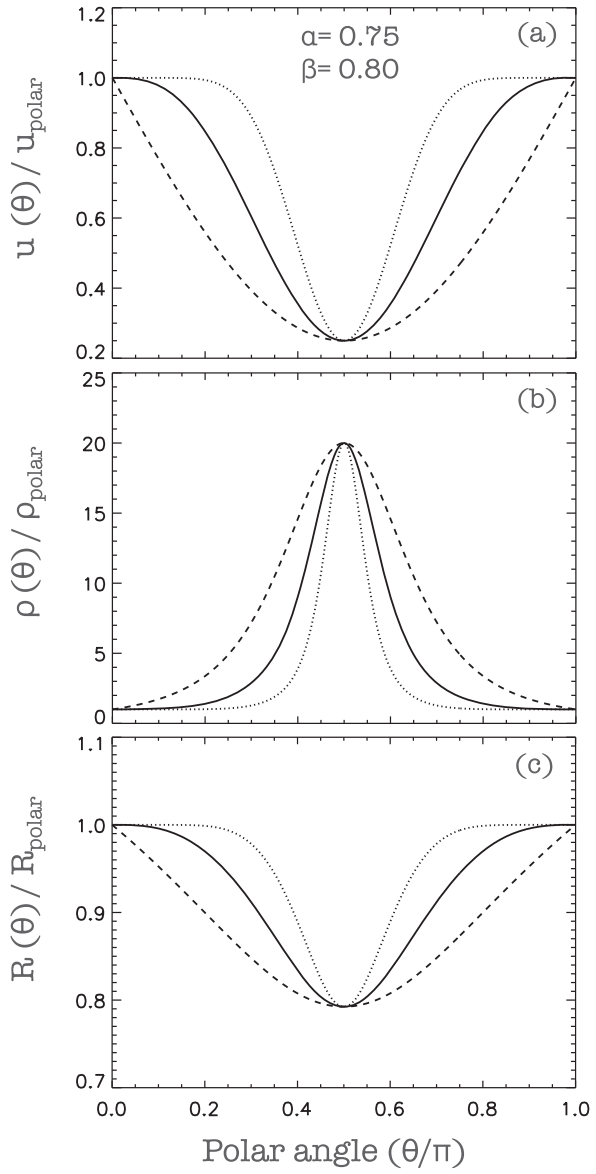

Figure 2. The bipolar distribution of the CSM velocity (a), density (b) and outer radius (c), normalized over their polar values. The graphs are described by equations (1), (2) and (3), assuming $\alpha = 0.75$ and $\beta = 0.8$. The solid lines correspond to $k = 3$, while the dashed and dotted lines denote $k = 1$ and $k = 6$, respectively.

structure. Following Weaver et al. (1977), the outer radius of an adiabetically expanding wind bubble R_b is proportional to $R_b \propto (L_w/n_{ism})^{1/5} t^{3/5}$, where L_w is the wind mechanical luminosity ($L_w = 1/2 \dot{M} u_w^2$), n_{ism} is the ISM density and t is the age of the bubble. Thus, the ratio of the wind bubble radii in two different polar angles (θ_1 and θ_2) at a given time is

$$\frac{R_b(\theta_1)}{R_b(\theta_2)} = \left[\frac{\dot{M}(\theta_1)}{\dot{M}(\theta_2)}\right]^{1/5} \left[\frac{u_w(\theta_1)}{u_w(\theta_2)}\right]^{2/5} . \quad (3)$$

Applying in equation (3) the adopted trigonometrical descriptions of the wind properties (equations 1 and 2), the ratio of the wind bubble radius at the equator over those at the poles is given by

$$\frac{R_{b,eq}}{R_{b,pol}} = (1-\alpha)^{2/5} (1-\beta)^{-1/5} . \quad (4)$$

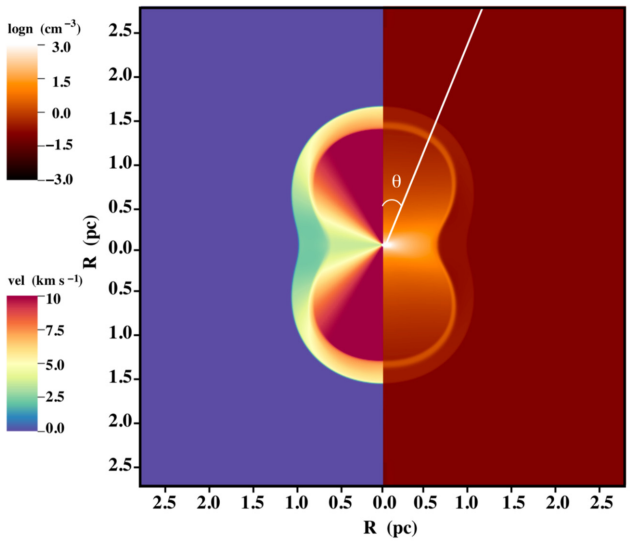

Figure 3. The 2D profile of a bipolar circumstellar structure. The stellar wind emanates from the axis origin where we impose an equatorially confined flow to enter the grid. The right plot shows the 2D density profile while the left displays the velocity distribution of the circumstellar structure. The wind and ISM parameters that we use are summarized in Table 1.

Table 1. The wind and ISM parameters adopted for the simulation of the bipolar CSM illustrated in Fig. 3. Here, n_{ism} and T_{ism} are the density and temperature of the ISM, while $\dot{M}_p$ and $u_{w,p}$ denote the wind mass-loss rate and terminal velocity at the poles, respectively. T_w and τ_w stand for the wind's temperature and the time interval of the wind phase and, finally, α, β and k are the constants used in the trigonometrical functions (equations 1 and 2).

Bipolar wind properties			
n_{ism} (cm^{-3})	0.1	α	0.75
T_{ism} (K)	1000	β	0.8
$\dot{M}_p$ (M$_\odot$ yr^{-1})	2×10^{-6}	k	3
$u_{w,p}$ (km s^{-1})	10	$u_{w,eq}/u_{w,p}$	0.25
T_w (K)	1000	ρ_{eq}/ρ_p	20
τ_w (Myr)	0.15	$R_{b,eq}/R_{b,p}$	0.79

Hence, according to equation (4), as the constant α increases and β decreases, the equatorial dense waist of the CSM becomes narrower with respect to the overall size of the bubble (see Fig. 2c).

Fig. 3 illustrates a typical bipolar circumstellar structure, as found by our simulations. The parameters that we use for the equatorially focused stellar wind are given in Table 1. The resulting circumstellar structure reveals an hourglass morphology, forming an equatorial disc of dense, slow-moving material. From inside out, the four main regions of the wind bubble are clearly depicted: the freely expanding wind where $\rho_{wind} \propto r^{-2}$; the shocked wind shell; the shell of shock ambient medium; and the outermost region of unperturbed ISM. The inner density jump corresponds to the position of the termination shock, while the outer one corresponds to the position of the forward shock. The equatorial to polar density and velocity ratios of the CSM are $\rho_{eq}/\rho_{pol} = 20.0$ and $u_{w,eq}/u_{w,pol} = 0.25$, respectively. Finally, the extracted relative ratio of the structure's outer radii in the poles and the equator is $R_{b,eq}/R_{b,pol} = 0.7$, which is ∼10 per cent smaller than the prediction of the analytical approach (see equation 4). This difference is attributed to radiation cooling that occurs in the dense equatorial region of the bipolar CSM.

2.2 Interaction of the SNR with the bipolar CSM and the formation of 'ears'

To model the interaction of a SNR with a bipolar CSM, we introduce the SN ejecta in the centre of the circumstellar structure depicted in Fig. 3, and we let the SNR evolve and interact with the surrounding medium. The adopted energy of the SN is 10^{51} erg, while the ejecta mass 1.38 $M_{\odot}$. Finally, following Truelove & McKee (1999), the ejecta density profile is described by a constant density core with an envelope that follows a power law of $\rho \propto r^{-n_{SN}}$ with $n_{SN} = 7$, while the ejecta's velocity increases linearly.[1]

Fig. 4 shows the 2D density and velocity contours for a sequence of snapshots of the SNR evolution, as found by our hydrodynamic simulations.

At the initial phase of the SNR evolution, the remnant is expanding within the circumstellar bubble (Fig. 4a). At the equatorial plane of the SNR, the forward shock encounters denser material than the rest of the remnant, and thus it expands more slowly. Consequently, the SNR starts to depart from the spherical symmetry and it reveals a bipolar morphology.

Around 60 yr after the SN explosion (Fig. 4b), the forward shock reaches the outermost region of the equatorial disc and starts to propagate at the surrounding ISM. The shock breakout from the CSM is accompanied by a significant acceleration of the forward shock at this portion of the SNR, as a result of the low density of the ISM and the high post-shock pressure. The SNR is expanding in the equatorial region with a velocity of $\simeq 1.5 \times 10^4$ km s^{-1}, while the rest of the remnant that remains within the bubble has an expansion velocity of $\simeq 9 \times 10^3$ km s^{-1}. As a result, a high-velocity protrusion is formed in the equatorial region of the SNR.

After 80 yr of evolution, the SNR has entirely swept up the CSM and starts to expand into the homogeneous ISM (Fig. 4c). The SNR's reverse shock carries on its morphology signatures of the interaction history with the bipolar CSM, which is more evolved in the equatorial plane of the SNR. The forward shock is accelerated and starts to establish a more spherical shape. Nevertheless, at the equator of the remnant, the initially formed protrusion retains its high velocity and forces the remnant to shape a local bulge.

As the SNR progresses further, the shocked gas behind the formed shock starts to decelerate and the remnant's contact discontinuity is subject to Rayleigh–Taylor (RT) instability (Figs 4d–f). After their initial growth, the formed RT fingers reach saturation and subsequently they become deformed, bend and finally fall back. The maximum size they reach is about half the width of the shocked shell, and thus they do not perturb the forward shock during the whole SNR evolution (see also Chevalier, Blondin & Emmering 1992). An intriguing exception is the RT finger formed at the equator of the remnant. This RT finger maintains its radial shape and extends up to the level that penetrates and deforms the shocked shell behind the forward shock and shapes an 'ear' into the overall SNR morphology. The formed equatorial 'ear' is maintained in full growth for about 1000 yr.

After that period of time, the 'ear' starts progressively to be swallowed by the main shell and the remnant approaches a spherical symmetry (Figs 4g and h). The equatorial RT finger is homogenized and dissipates within the surrounding gas, and thus it starts to be hardly distinctive. Finally, after 2800 yr of evolution, the lobe has been entirely engulfed within the remnant (Fig. 4i). At that moment, the reverse shock has reached the centre of the SNR while the forward shock has almost established a spherical shape. Thus, information about the CSM interaction is no longer carried by the SNR.

[1] The adopted SN properties correspond to a normal, Chandrasekhar-mass SN Ia explosion. In Section 2.4, we extend our model for cases more relevant to core collapse SNe.

2.3 Mechanism for the formation of 'ears'

To further explain the formation and preservation mechanism of the extended equatorial RT finger (i.e. the mechanism responsible for the genesis and evolution of the SNR 'ears'), we illustrate in Fig. 5(a) the snapshot of the SNR evolution at $t_{SNR} = 400$ yr (i.e. the same as Fig. 4d) but zoomed-in to the region of the lobe. In this plot, the 2D density contours are accompanied by the velocity vectors of the gas. In addition, in Fig. 5(b), we present the 2D contours of the SNR shocked gas pressure.

As depicted in these plots, the initial rapid expansion of the SNR equatorial bulge and its propagation in the low-density ISM causes a substantial drop of the post-shock pressure. As the pressure behind the lobe becomes lower than that of the neighbouring gas, an angular pressure gradient is established, which in turn triggers a tangential component at the shocked gas velocity towards the equator of the remnant. This tangential flow converges at the equatorial RT finger, supporting it to maintain its radial structure and grow further. The velocity of the gas that consists the RT finger is higher than that of the surrounding flow. As a result, a Kelvin–Helmholtz instability grows at the outer part of the finger, forming an arrow-shaped tip. The compressed gas between the equatorial RT finger and the SNR's forward shock forces the latter to gain and retain its 'ear' morphology from several hundreds up to a few thousand years after the SN explosion.

Finally, Fig. 5(c) illustrates the spatial distribution of the three components that constitute the resulting SNR: the SN ejecta, the swept-up wind material and the shocked ISM. Overall, as expected, the SN ejecta dominates in the inner region of the SNR surrounded by the shocked wind material that has accumulated into a thin shell. The outer layer of the SNR consists of the shocked ISM that is lying behind the remnant's forward shock. The three layer stratification is disturbed by the RT instabilities, where a partial mixing between the three components occurs in the region of the contact discontinuity. In the area where the lobe has been shaped, a different image emerges. Because of the equatorially confined circumstellar structure that was surrounding the explosion centre, a large amount of CSM material has been assembled into a thick dense region just behind the region of the lobe and substantial mixing occurs between the CSM and SN ejecta material. Finally, the extensive RT finger in the equator consists almost exclusively of CSM material surrounded by the shocked ISM.

2.4 Comparison of models

In this section, we evaluate differences in the morphology and properties of the 'ears' formed in SNRs by varying the main physical variables involved in the model. Given that the final outcome is determined by the combination of the SN, CSM and ISM properties, the overall parameter space in our modelling is immense. For this reason, we restrict our study by focusing on the SN explosion properties, the stellar wind properties and, finally, those of the CSM bipolarity. In particular, we have produced seven different models (in addition to the model presented in Section 2.2, hereafter called Model A) by varying: (i) the SN ejecta mass and density power-law index; (ii) the stellar wind mass-loss rate; and (iii) the bipolar CSM density and velocity distribution as defined by the constants α, β and k (see equations 1 and 2). The parametric space we examined was

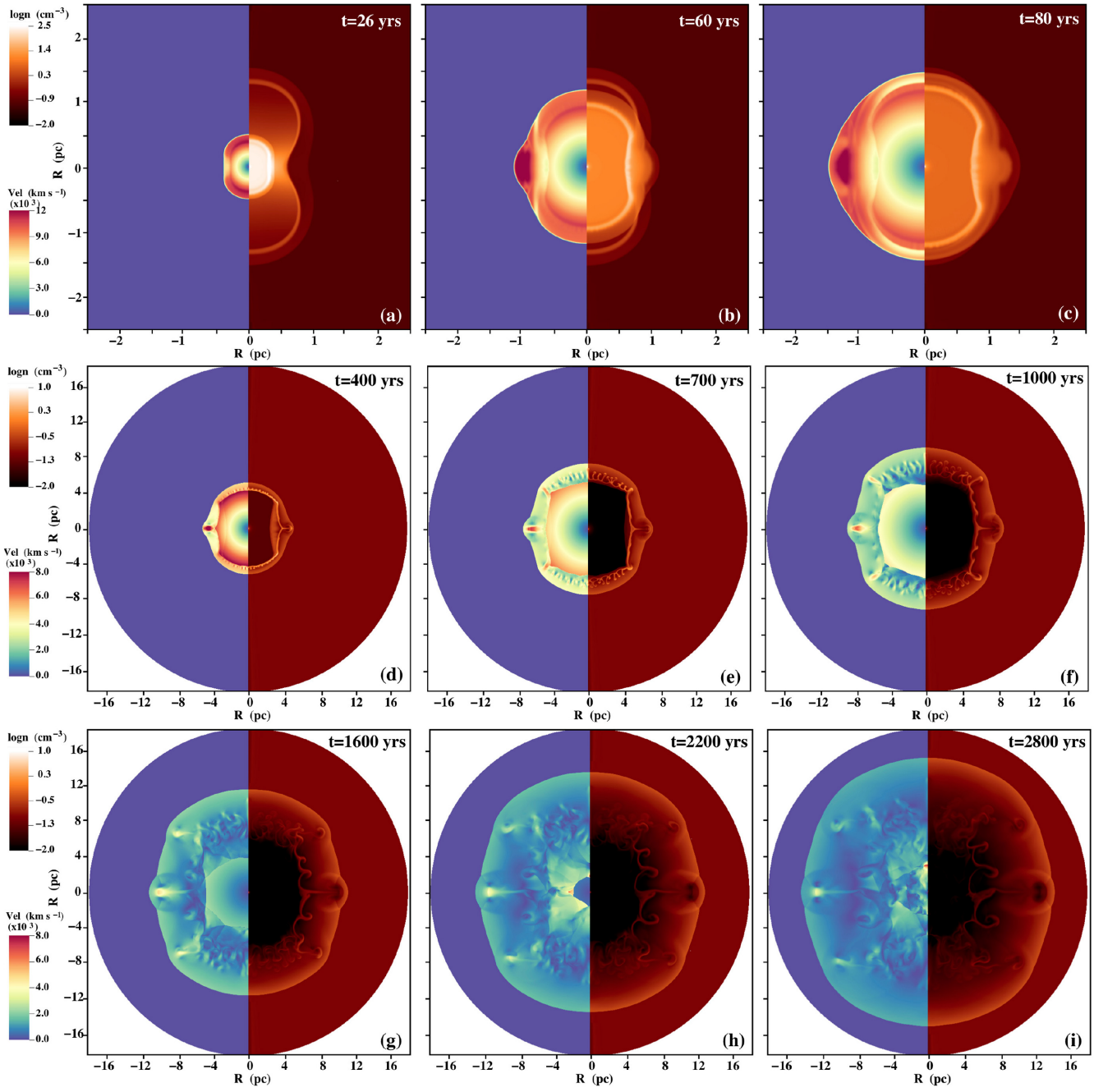

Figure 4. The evolution of the SNR as a result of the interaction of the SN ejecta with the bipolar circumstellar structure of Fig. 3. The right part of each plot depicts the 2D density contours of the SNR while the left part shows the corresponding gas velocity. The time indicates the age of the SNR at each snapshot. Note that both the axis and colour scale in the first row are different to the other two rows.

centred on Model A, whereas the other seven models were produced by changing one of the aforementioned variables each time.

The properties adopted for the eight models are summarized in Table 2. Fig. 6 illustrates the CSM density and velocity distribution at the moment of the SN explosion, while Fig. 7 presents the resulting SNR, for each model, at two different snapshots: t_{SNR} = 700 yr (Fig. 7, panel I) and t_{SNR} = 1600 yr (Fig. 7, panel II). The main conclusions resulting from our hydrodynamic simulations and the subsequent comparison among the models are the following.

2.4.1 *Varying the SN explosion properties (Models B and C).*

In this set of models, we kept the bipolar CSM structure the same as in Model A (Fig. 6a) and we changed the SN explosion properties. We first increased the SN ejecta mass from 1.38 to 7 $M_{\odot}$ (Model B) and, subsequently, we ran an additional model with a higher power-law index of the SN density profile (n_{SN} = 11; Model C). The adopted parameters of Model B could potentially correspond to a Type Ib/c SN, with those of Model C corresponding to a Type II event, as the latter are characterized by steeper outer density profiles (Chevalier 1982b).

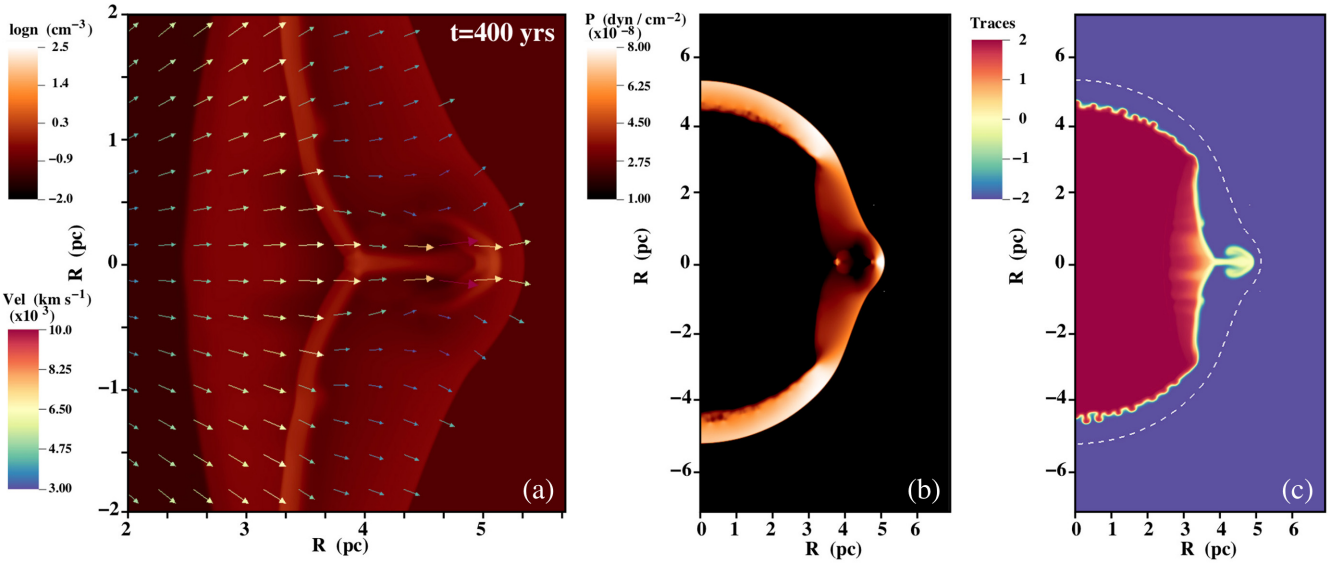

Figure 5. (a) The same snapshot of the SNR as in Fig. 4(d) but zoomed-in to the region where the 'ear' is formed. In addition, the velocity vectors of the flow have been added. (b) The 2D gas pressure contours of the SNR at the same age. (c) The traces of three components that constitute the SNR: the SN ejecta, the circumstellar material and the ISM. The values close to 2 indicate pure SN ejecta material, those around zero refer to regions where the CSM material dominates and, finally, these close to –2 refer to regions of the grid of purely interstellar material. The values between these numbers correspond to regions where mixing among the three components occurs. The dashed line indicates the position of the SNR forward shock in this specific snapshot.

Table 2. The eight studied SNR models interacting with bipolar circumstellar structure. The first column gives the model's name and the second column the parameter that has been changed with respect to Model A. Columns (3)–(8) display the adopted parameters of each model where the changed parameters are denoted in bold. Finally, columns (9) and (10) give the figure number where the CSM and SNR of each model are illustrated, respectively. In all models, we considered an ISM density of $n_{\rm ism} = 0.1$ cm^{-3} and temperature $T_{\rm ism} = 1000$ K, while we let the CSM bubble evolve for $\tau_{\rm w} = 0.15$ Myr, adopting a polar wind velocity of $u_{\rm w,p} = 10$ km s^{-1}.

		Comparison of the properties of the models							
Model name	Parameter changed	$M_{\rm SN}$ (M$_\odot$)	$n_{\rm SN}$ (cm^{-3})	$\dot{M}_{\rm p}$ (M$_\odot$ yr^{-1})	k	α	β	CSM	SNR
(1)	(2)	(3)	(4)	(5)	(6)	(7)	(8)	(9)	(10)
A	–	1.38	7	2×10^{-6}	3	0.75	3	Fig. 6(a)	Fig. 7a)
B	Total SN ejecta mass	**7**	7	2×10^{-6}	3	0.75	0.8	Fig. 6(a)	Fig. 7(b)
C	SN density power-law index	**7**	**11**	2×10^{-6}	3	0.75	0.8	Fig. 6(a)	Fig. 7(c)
D	Stellar wind mass-loss rate	1.38	7	$\mathbf{1 \times 10^{-5}}$	3	0.75	0.8	Fig. 6(b)	Fig. 7(d)
E	CSM equatorial confinement	1.38	7	1.5×10^{-6}	**1**	0.75	0.8	Fig. 6(c)	Fig. 7(e)
F	CSM equatorial confinement	1.38	7	2.3×10^{-6}	**6**	0.75	0.8	Fig. 6(d)	Fig. 7(f)
G	CSM polar to equatorial ratios	1.38	7	2.4×10^{-6}	3	**0.65**	**0.7**	Fig. 6(e)	Fig. 7(g)
H	CSM polar to equatorial ratios	1.38	7	1.4×10^{-6}	3	**0.85**	**0.9**	Fig. 6(f)	Fig. 7(h)

The SNR resulting from Model B is depicted in Fig. 7(b), in panels I and II. Because of the higher ejecta mass, compared with Model A, the SNR evolves more slowly while the shocked ejecta shell and the freely expanding ejecta region reveal higher densities. Within the time-scales of our simulations, no substantial deceleration occurs in the SNR and the reverse shock remains relatively close to the contact discontinuity. As a result, the growth of the RT instabilities remains limited. The equatorial RT finger displays a similar behaviour as in Model A, as it is radially extended and forces the remnant to shape a local 'ear'. After its initial growth (Fig. 7b, panel I), the lobe starts progressively to be merged within the shocked ambient medium shell (Fig. 7b, panel II). Nevertheless, contrary to Model A, in Model B the local lobe dissipates when the SNR is still in the free expansion phase where the reverse shock is still active. In conclusion, for given CSM conditions, by changing the SN ejecta mass, no essential differences are expected to the morphology and properties of the 'ears'. However, as the SN mass increases, the whole process of the formation, growth and dissipation of 'ears' occurs in prior stages of the SNR evolution.

In Model C, we additionally increased the power-law spectral index of the SN density profile ($n_{\rm SN} = 11$). As is clearly illustrated in Fig. 7c (panels I and II), the formed lobe is smaller in size compared with Models A and B, while after 1600 yr it is hardly distinctive. Such a result is expected as by increasing the SN density power-law index, the dependence of the SNR expansion velocity on the CSM density becomes weaker (Blondin et al. 1996; Chevalier 1982a). Thus, the CSM density enhancement at the equator has moderate effects on the evolution of the subsequent SNR and, as a result, the phenomenon of the formation of 'ears' is mitigated.

2.4.2 *Varying the stellar wind properties (Model D).*

In Model D, we kept the same SN properties and the constants α, β and k that determine the CSM bipolarity as in Model A but

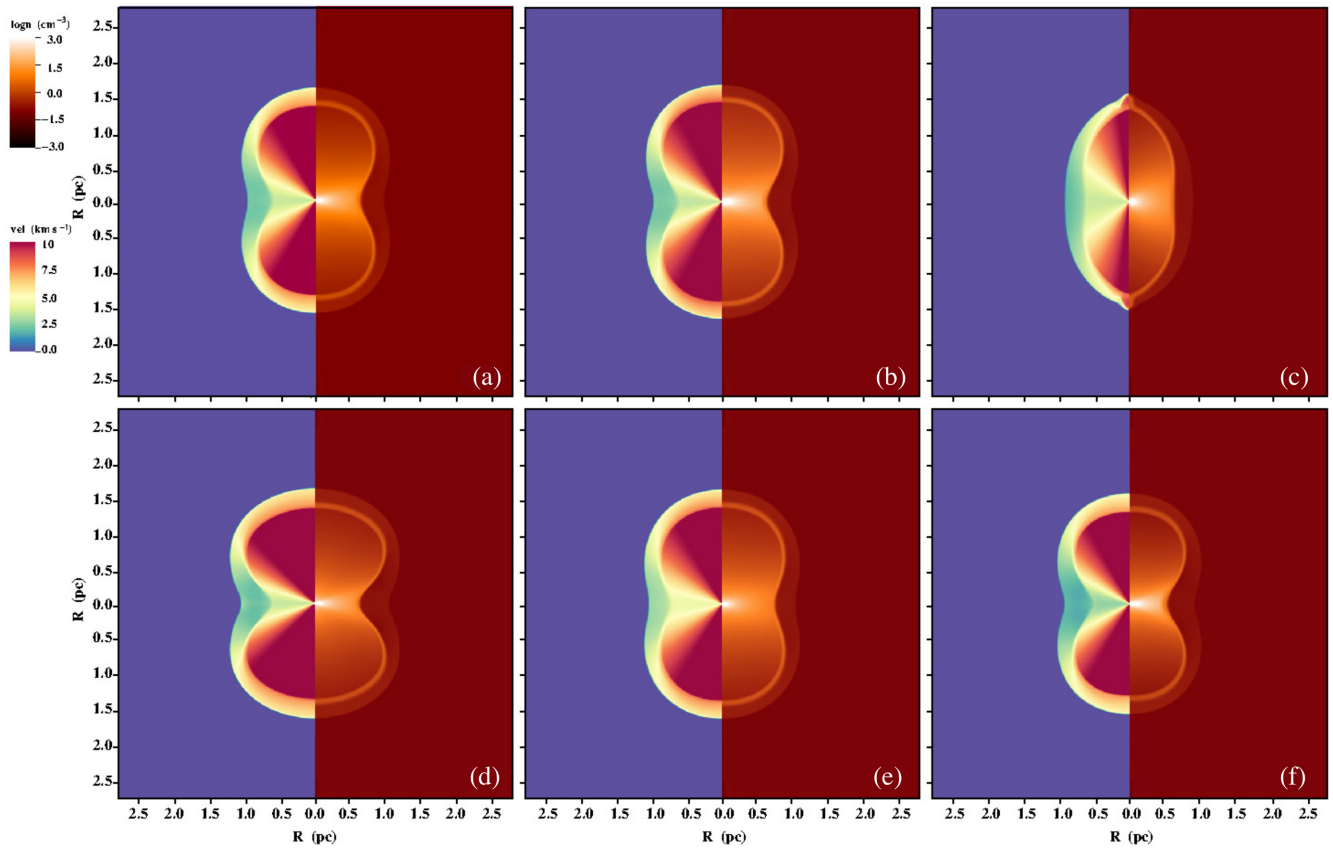

Figure 6. The 2D density and velocity contours of the CSM at the moment of the SN explosion. (a) The CSM that corresponds to Models A, B and C. (b)–(f) The resulting CSM of Models D, E, F, G and H, respectively (see Table 2 and text for details).

we increased the stellar wind mass-loss rate by five times ($\dot{M}_{\rm p} = 10^{-5}$ M$_{\odot}$ yr^{-1}). As expected, the resulting CSM (Fig. 6b) retains the same structure but it is denser and slightly more extended than the CSM of Model A.

The resulting SNR of Model D is illustrated in Fig. 7d (panels I and II). Compared with Model A, there are two main distinctive differences. The first is the formation of a fast moving reflected shock, triggered by the collision of the SNR with the density walls of the wind bubble, which rapidly approaches the centre of the remnant. The morphology of the reflected shock follows that of the wind bubble, as it is more evolved at the SNR's equator where a large amount of shocked CSM material has been accumulated. The second difference compared with Model A concerns the properties of the 'ears'. The higher density contrast between the circumstellar structure and the surrounding ISM results in a stronger shock breakout of the SNR. The high post-shock pressure of the swept-up CSM at the equatorial plane of the remnant is higher and, consequently, a more profound and extended lobe is formed at the resulting SNR. The shaped 'ear' preserves its structure for a much larger time interval, surviving until the end of our hydrodynamic simulations (i.e. $t_{\rm SNR} = 2800$ yr).

2.4.3 Varying the properties of the CSM bipolarity (Models E–H).

In the sequence of Models E–H, we study the dependence of the resulting SNR properties on the level of bipolarity of the surrounding CSM. For this purpose, we kept the same SN properties as in Model A. In addition, we normalized the stellar wind mass-loss rate of each model in order to maintain the same total mass of the stellar wind enclosed in the CSM bubble, as for Model A.

In Models E and F, the polar to equatorial CSM density and velocity ratios are the same as in Model A (i.e. we kept the same α and β) but we changed the confinement level of the equatorial disc by adopting $k = 1$ and 6, respectively.

Because of the low equatorial wind confinement of Model E, the resulting wind bubble deviates from the bipolar morphology and displays an elliptical shape where the radius, the density and the velocity of the CSM change smoothly from the poles to the equator (Fig. 6c). The interaction of the subsequent SNR with such a circumstellar structure is not able to form local equatorial lobes. Instead, the remnant presents a small bulge on its equator (Fig. 7e, panel I) that after 1600 yr has completely disappeared (Fig. 7e, panel II).

By contrast, the high value of k imported in **Model F** results in a bipolar CSM structure characterized by a narrow equatorial waist of dense, slow-moving material (Fig. 6d). Comparing the resulting SNRs of Models A and F, there is no noticeable difference regarding the size, the geometry and the life duration of the formed 'ears'. Nevertheless, a novel feature that emerges from the SNR of Model F is the formation of two additional extended RT fingers that arise antisymmetrically to the equatorial one at about $\theta = 60^{\circ}$ and 120° (Fig. 7f, panel I). Similar to their equatorial counterpart, the two RT fingers penetrate the shell of the shocked gas, deform the SNR forward shock and, finally, shape two additional lobes on the overall morphology of the remnant (Fig. 7f, panel II).

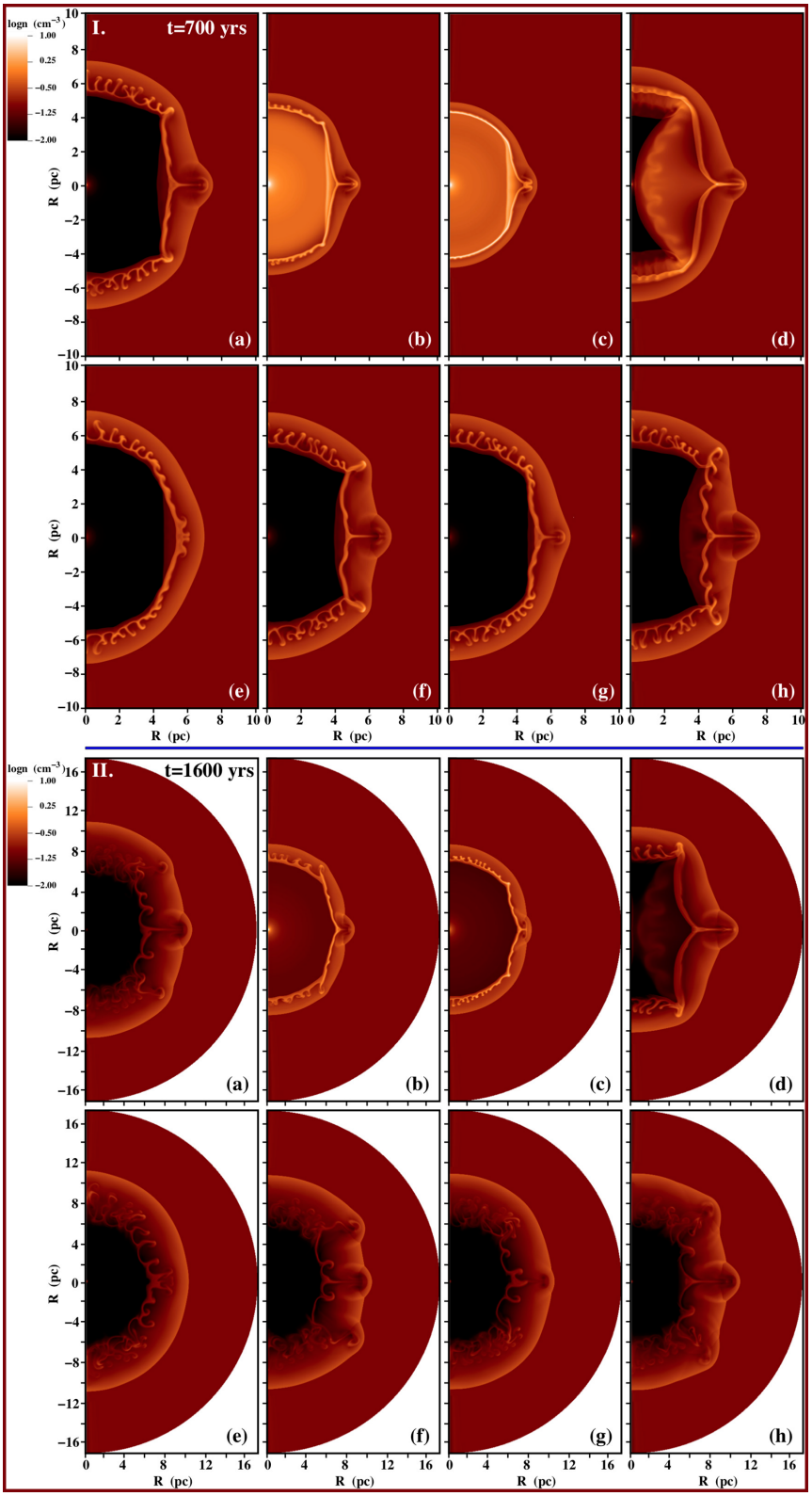

Figure 7. The 2D density contours of the SNR for Models A–H. The upper panel of plots (I) corresponds to the SNR age of $t = 700$ yr, while the lower panel is for $t = 1600$ yr. See Table 2 and text for details.

The formation of these two RT fingers, which are also present in the rest of the models but to a lower extent, is attributed to the obliquity of the reverse shock to the freely expanding SN ejecta at the point where the CSM bubble bends to form the equatorial waist. As shown also by Blondin et al. (1996), the non-frontal collision of the freely expanding ejecta with the reverse shock provokes strong vorticity on the post-shock flow, which in turn supports the growth of an extended RT instability.

The final models of the studied set are Models G and H. In these models, the parameter that has been changed, compared always with Model A, is the ratio of the CSM density and velocity from the poles to the equator, as defined by the constants α and β.

Fig. 6(e) shows the CSM of Model G. Because of the low α and β values imported in this model, the wind bubble reveals a moderate bipolar shape with an equatorial radius that is ∼20 per cent smaller than the polar radius. Even if the required criteria for such a circumstellar structure are met for the formation of 'ears' on the resulting SNR, the formed lobe is hardly distinguished after 700 yr of evolution (Fig. 7g, panel I) and it is completely engulfed within the shocked ambient medium shell after 1600 yr (Fig. 7g, panel II).

Finally, Fig. 6(f) illustrates the CSM of Model H, characterized by a typical elongated hourglass shape with a narrow, dense waist. The interaction of the SN ejecta with this circumstellar structure shapes a sizeable 'ear' much larger in both length and width compared with Model A (Fig. 7h, panel I). Furthermore, the two additional lobes seen in Model F are also present in Model H (Fig. 7h, panel II). However, the position of the two additional lobes is shifted more towards the poles of the remnant (placed at $\theta = 50^\circ$ and 130°), while they remain smaller than the equatorial lobe.

3 DISCUSSION

3.1 Comparing the model results to the relevant observations

We have argued that the 'ears' observed in several SNRs were formed by the interaction of the SN ejecta with a bipolar CSM that occurred during the early phases of SNR evolution. Using hydrodynamic simulations, we intended to present the physical mechanism lying behind the formation of 'ears' and to demonstrate the dependence of the final outcome on the SN/CSM properties. Thus, in our modelling we did not aim to model any specific SNR – a process that requires a thorough modelling and detailed fine-tuning of the imported parameters – whereas the chosen parametric space imported in our models was limited to a specific range that definitely cannot cover all cases of SNRs with 'ears'. Nevertheless, the results extracted by the set of models presented in this paper reveal a sequence of intriguing similarities with the properties of the 'ears' observed in nearby SNRs.

The first similarity regards the size of the formed 'ears'. In our models, the radius of the remnant is about 10 per cent to 65 per cent larger in the region of the formed lobe than its overall radius (with Model E revealing the smallest ear radius and Model H the largest). In the known sample of SNRs that have been observed to host 'ears' in their morphology (see Fig. 1; see also Tsebrenko & Soker 2015a; Bear et al. 2017), the nebula's radius at the region of the lobe has a length up to ∼30–50 per cent more than the radius of the main shell, which is well within the range of our extracted results. The same applies for the time-scales of the lifespan of the 'ears' resulting from our modelling. We have shown that the 'ears' start to be formed about 100 yr after the SN explosion (Fig. 4c) and, in many cases, they survive until the end of our hydrodynamic simulation (i.e. $t_{\rm SNR} =$ 2800 yr). This time range covers most of the ages of SNRs observed to reveal 'ears' in their morphology. The exception is the SNR S147 whose kinematical age is estimated to be about an order of magnitude larger (Kramer et al. 2003). This means that either S147 encountered a much larger and/or denser circumstellar structure than the SNRs presented in this work or another physical mechanism was responsible for the formation of its 'ears' (see Section 3.3).

Our modelling extracted a range of morphologies for 'ears' depending on the selected CSM/SN properties and/or the evolutionary phase of the SNR. In particular, it has been shown that when the SNR is still young ($80 < t_{\rm SNR} < 400$ yr; see Fig. 4c) or the CSM is characterized by a modest density gradient from the poles to the equator (Models E and G; Figs 7e and g) the resulting 'ear' appears as a bulge of an almost triangular shape that progressively starts to protrude as we move towards the equator of the remnant. By contrast, for the cases where the SNR is older than ∼400 yr (Figs 4d–f) and for CSM structures that display a well-confined, narrow and dense equatorial waste (e.g. Models D and H; Figs 7d and h), the formed 'ears' reveal the morphology of a localized lobe that inflates out of the SNR's main shell. The former morphology (triangular shape) is more similar to that observed in the very young ($t \sim 100$ yr) SNR G1.9+0.3, while the latter (local lobe) is met in most SNRs with 'ears', such as Kepler's SNR, G309.2–06 and S147 (see Fig. 1).

Another point shown by our simulations is that during the early phases of the formation of 'ears' ($t_{\rm SNR} < 700$ yr) the remnant's forward shock in the region of the lobe is faster than the overall expansion velocity of the SNR. Such a result is aligned to the bright X-ray synchrotron emission observed in front of the 'ears' for the young SNRs, Kepler's SNR (Vink 2008) and G1.9+0.3 (Borkowski et al. 2017). This indicates that the remnants reveal high expansion velocities in these regions. Regarding Kepler's SNR, there is another interesting similarity to the results of our modelling. X-ray and infrared observations of the remnant – see Burkey et al. (2013) and Williams et al. (2012), respectively – have shown that the central regions of the SNR are occupied by dense, shocked CSM material, which is lying on a strip roughly along the site that connects the two 'ears'. As we have shown in Fig. 5(c), our models predict the accumulation of a large amount of CSM at the equator of the remnant (i.e. where the two 'ears' are sculptured), in agreement with what is observed for Kepler's SNR.

Finally, an interesting feature resulted by our modelling is that under specific CSM conditions (Models F and H), apart from the equatorial lobe, two additional lobes are formed in the final morphology of the remnant. Intriguingly, such a three-lobe structure has been observed in the south-west region of the Large Magellanic Cloud, for SNR DEM 34A (Meaburn 1987). This was attributed by Meaburn to local inhomogeneities within the parent sheet or alternatively to the collision of the blast wave with a helical annulus. Our model offers an alternative explanation for the formation of the three-lobe structure observed in DEM 34A. The same applies for the case of N63A, which reveals a multilobe morphology consisting of 'crescent'-shaped lobes of several sizes (Warren, Hughes & Slane 2003). Of course, as mentioned above, detailed modelling – most likely involving extra ingredients than the axisymmetric model presented here – is required in order to reproduce the 'exotic' morphologies of the aforementioned SNRs.

3.2 Bipolar CSM structures around SN progenitors

The fundamental assumption of our model is that the centre of the SN explosion is surrounded by a dense circumstellar bubble characterized by a bipolar morphology and density enhancement

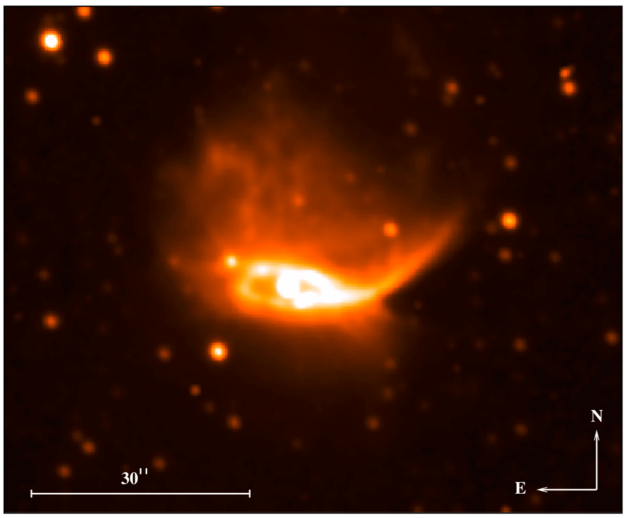

Figure 8. An Hα image of the bipolar PN Henize 2-428 as observed by the 2.3-m Aristarchos telescope at Helmos Observatory (Greece) on 2015 November 12. The detector was a 2048 × 2048, 13.5-μm pixel CCD, with a field of view of 5.5 × 5.5 arcmin^2 (0.32 arcsec pixel^{-1} in binning 2 × 2), while the exposure time was 1800 s.

at its equatorial plane. The existence of such CSM structures is predicted by the stellar evolution theory and has been confirmed by numerous observations.

Indeed, a significant fraction of evolved stars, throughout the Hertzsprung–Russell diagram, have been found to be engulfed by nebulae that possess bipolar symmetry. These circumstellar structures are characterized by dense equatorial discs, rings or tori that form a narrow, dense waist around the central star and two extended polar cups that are lying perpendicular to the equatorial plane (e.g. Fig. 8). The physical processes responsible for the formation of the bipolar nebulae around evolved stars are still debatable. Stellar rotation (e.g. Bjorkman & Cassinelli 1993; Heger, Langer & Woosley 2000), close binary interactions (e.g. Mastrodemos & Morris 1999; Huggins, Mauron & Wirth 2009; Politano & Taam 2011), eruptive mass loss (e.g. Smith & Arnett 2014) and magnetic fields (e.g. García-Segura et al. 1999; Matt & Balick 2004; Townsend & Owocki 2005) have been suggested as the most eminent mechanisms to explain the stellar outflows confinement towards the equator and the formation of bipolar circumstellar structures.

Regarding the high stellar mass regime, the types of stars that have most frequently been found to be surrounded by bipolar CSM are luminous blue variables (LBVs; e.g. η Carinae; Smith 2002) and blue supergiants (BSGs; e.g. SBW1, SBW2; Smith, Bally & Walawender 2007). Indications of bipolar and/or disc-like CSM morphologies are also seen in colder massive stars such as yellow supergiants (YSG) and evolved red supergiants (RSGs) such as IRC+10420 (Tiffany et al. 2010). Given that all these types of stars are potential core collapse SN progenitors, it is expected that a percentage of SNe occur within bipolar circumstellar structures and subsequently interact with them. The most characteristic example of such an SN explosion is SN 1987A (West et al. 1987), a Type II SN with a BSG progenitor (Hillebrandt et al. 1987). The CSM around this SN shows a dense equatorial ring surrounded by two polar cups (Crotts & Heathcote 1991; Plait et al. 1995). Intriguingly, the CSM of SN 1987A is almost identical to that found around the B1.5Ia supergiant Sher 25 (Brandner et al. 1997) and the Galactic LBV HD168625 (Smith 2007). Other cases of core collapse SNe that show evidence of interaction with dense bipolar structures are the Type IIn SNe SN 2010jl (Katsuda et al. 2016) and SN 2009ip (Mauerhan et al. 2014; Reilly et al. 2017), for which it has been suggested that they originated from an LBV progenitor. SN 1998S is additional observational evidence of a Type IIn CC SN with a bipolar CSM coming most likely from an evolved red or yellow supergiant star (Chugai 2001).

As far as low-mass stars are concerned, signs of aspherical CSM that display bipolar symmetry are mostly found in PNe, such as MyCn 18, Hb12 and Mz 3 (see O'Connor et al. 2000; Clark et al. 2014; Clyne et al. 2015, respectively). Very recently, using the Atacama Large Millimeter/submillimeter Array (ALMA), a sample of stars in the asymptotic giant branch (AGB) phase was observed in high resolution, and it was found that their winds sculpt non-spherical circumstellar structures that share common properties with those of PNe (i.e. bipolar symmetry hosting a density-enhanced equatorial waist; Decin et al. 2020). AGB stars have been proposed as possible candidates for the donor stars of SNe Ia progenitor systems, especially for cases where these cosmic explosions reveal Hα narrow emission lines during their early spectra (e.g. SN 2002ic; Hamuy et al. 2003). In addition, there is growing theoretical and observational evidence in the literature showing that a fraction of SNe Ia occur in the centres of PNe shaped by their progenitor systems (Santander-García et al. 2015; Tsebrenko & Soker 2015c; Cikota et al. 2017; Chiotellis, Boumis & Spetsieri 2020). Thus, apart from their core collapse counterparts, SNe Ia are also likely to occur within, and subsequently interact with, a bipolar CSM.

Finally, indirect evidence of SN interaction with bipolar circumstellar structures is shown through the observables we receive from a number of nearby SNRs. It has been suggested that their non-spherically symmetric morphology, kinematics and emission properties can best be explained if the progenitor stellar system had mass outflows confined more to the equatorial plane than along the poles (Igumenshchev, Tutukov & Shustov 1992; Gaensler et al. 1998; Burkey et al. 2013).

All the aforementioned evidence points towards the plausibility of our SNR 'ear' formation model in nature, as they advocate for the fact that a non-negligible percentage of SNe (both core collapse and Type Ia) are surrounded by equatorially confined bipolar CSM. The second important assumption of our model is that the formed circumstellar structures are denser than the ambient medium. This condition is required for the SNR shock breakout, which in the framework of our model is the central engine for the formation of the two antisymmetric 'ears'. Hence, our model is more aligned to SN progenitors, which suffer from intense and slow mass outflows during the final phases of their evolution. In conclusion, if indeed the two lobes in a SNR have been formed under the physical process suggested in this model, the most plausible progenitor of the remnant is a LBV or a YSG/RSG star for the case of core collapse SNe, and a symbiotic binary system or a PN for SNe Ia. Nevertheless, other important factors such as stellar duplicity and/or the involvement of magnetic fields can substantially alter the evolution and mass outflows properties of the progenitor system, and thus broaden the spectra of stellar candidates suggested above.

3.3 Comparison with the jet and the model of Blondin et al.

We have presented evidence that the antisymmetric 'ears' observed in a number of SNRs could potentially be sculpted through the SNR shock breakout from a bipolar CSM that was surrounding the centre of the SN explosion. This scenario is placed as a third alternative to the other two outstanding 'ears' formation models suggested in

the literature: (i) the jet model, which suggests that the 'ears' are shaped by the interaction of the SNR with two jets launched by the progenitor system (e.g. Tsebrenko & Soker 2013) and (ii) the model of Blondin et al. (1996) in which the 'ears' are inflated during the evolution of the SNR within an axisymmetric and equatorially enhanced circumstellar structure.

These three ear formation models seem to be complementary rather than mutually exclusive, as they rely on different physical mechanisms that are independent from each other, and thus they are applicable to different systems. For instance, in a number of SNRs that reveal 'ears' in their morphology, one or two jets have been observed lying within the direction of the two opposite lobes (e.g. W50; Fabrika 2004). Such evidence points directly towards the jet formation model. However, evolved Type Ia SNRs are difficult to explain using the jet model as in the vast majority of SNe Ia explosions the white dwarf progenitor is completely destroyed (Livio & Mazzali 2018) so no stellar system remains to trigger a jet.

Luckily, there are two main differences among the three models, which to a large extent can make the physical origin of the formed 'ear' on SNRs distinctive. These two differences are the orientation of the formed protrusions with respect to the host SNR and the time-scales in which the ear formation process occurs regarding the SNR evolutionary phase.

3.3.1 Orientation of 'ears'.

In the model of Blondin et al. (1996), the two protrusions emerge along the polar axis of the SNR where the CSM displays the lowest density. Similarly, given that the jets are expected to be launched perpendicularly to the equator of the stellar system, the two 'ears' are more likely to be inflated close to the poles of the remnant. In this model, the two antisymmetric lobes are shaped in the equator of the SNR where the CSM is confined into a dense and narrow waist. Consequently, if the two lobes of a SNR have been formed by the shock breakout from a bipolar CSM (i.e. as suggested by this model), then a large amount of shocked CSM material is expected to be concentrated within a strip between the two 'ears' (as observed in the case of Kepler's SNR; see Section 3.1). By contrast, in Blondin et al. (1996) and the jet model, the region of the dense, shocked CSM should lie roughly perpendicular to the line that connects the two lobes.

3.3.2 Involved time-scales.

The model of Blondin et al. (1996) predicts that the two protrusions are formed when the SNR is within the axisymmetric circumstellar bubble. Thus, it is expected that two opposed 'ears' are shaped when the remnant is still in a very early evolutionary state. Such a model is sufficient to explain young SNRs such as 41.9+58 in M82 (Bartel et al. 1987), but it seems difficult to apply it to mature SNRs that have been evolved beyond the adiabatic phase (e.g. S147 and G309.2–0.6). However, the model presented in this work advocates that the two opposite lobes are sculpted when the remnant has utterly penetrated the circumstellar structure and starts to propagate into the ambient medium. The time interval in which the two 'ears' are present ranges from hundreds to thousands of years after the SN explosion, while for given SN/CSM properties it can last well beyond the Sedov phase. Hence, the two axisymmetric CSM models – that is Blondin et al. (1996) and the present model – cover complementary different evolutionary stages of SNRs. Finally, regarding the jet model, it is difficult to predict the phase in which the 'ears' are formed, given that two jets can be launched from the progenitor system at any time of the SNR evolution (Bear et al. 2017; Grichener & Soker 2017). Nevertheless, as mentioned above, for the case of Type Ia SNe the jets cannot be launched after the SN explosion, something that places strict spatial and temporal limits on the 'ear' formation process. In particular, the SNe Ia jet models (Tsebrenko & Soker 2013) suggest that the 'ears' were formed through the collision of either 'jet-carrying' SN ejecta with a spherical (pre-)PN shell or spherical SN ejecta with an 'ear-shaped' PN shell, depending on whether the jets are triggered during or prior to the explosion, respectively. Thus, according to these models the spatial scales for the 'ear' formation should be comparable to the size of the surrounding (pre-)PN. Given that the majority of PNe reveal a radius of $R_{\rm PN} \sim 0.05-1$ pc (Frew, Parker & Bojičić 2016), a similar spatial scale is imposed for the SNe Ia jet model.

4 SUMMARY

The results and the main conclusions of this work are summarized as follows.

(i) We have modelled the interaction of a SNR with a surrounding bipolar, equatorially confined circumstellar structure. We have shown that such an interaction can be responsible for the formation of two opposite lobes ('ears') frequently seen in the morphology of several SNRs.

(ii) According to our model, the 'ears' are formed by the SNR's forward shock breakout from the bipolar CSM. Because of the geometry of the SNR/CSM system, the post-shock flow converges at the equator of the remnant, something that supports the growth of an extended RT finger. This RT finger presses and deforms the SNR's forward shock, shaping a local lobe in the equator of the remnant. This lobe survives from hundreds to thousands of years after the SNR's shock breakout from the CSM.

(iii) We ran a set of models evaluating differences in the morphology and the properties of the formed SNR 'ears' by varying the CSM and SN properties. We found that both the size and the lifespan of the formed 'ears' increases with the following: the density contrast between the circumstellar bubble and the ambient ISM; the level of confinement of the circumstellar material at the equator of the system; and the ratio of the CSM polar density and flow velocity over the equatorial ones. Regarding the SN properties, we found that by increasing the ejecta mass, the 'ears' are present at earlier evolutionary stages of the SNR, while the protrusion is less pronounced for SNe characterized by sharp declining ejecta density profiles.

(iv) The results extracted from the grid of our hydrodynamic simulations reveal a number of similarities to the relevant observables regarding the size, the lifespan and the kinematics of the 'ears' in SNRs. In addition, our model predicts the accumulation of a large amount of shocked CSM in the region between the two antisymmetric lobes, something that has been observed in the case of Kepler's SNR. Finally, under specific CSM conditions, our modelling extracted SNRs possess six lobes in their morphology. Such multilobe features have been observed in a number of SNRs such as DEM 34A.

(v) We have presented theoretical and observational evidences of SN explosions occurring within a bipolar CSM adopted in our model. This fact enhances the plausibility of our model in nature. We have discussed the most possible progenitors of the SNRs that reveal two opposite lobes, under the framework of our model, suggested to be YSGs/RSGs or LBVs for the core collapse SNe and symbiotic binaries or PNe for thermonuclear SNe.

(vi) We compare our model with the other models of 'ear' formation suggested in the literature. We have shown that these models can be distinctive as they predict different orientations of the formed 'ears' with respect to the host SNR and different timescales in which the 'ear' formation process occurs.

ACKNOWLEDGEMENTS

This research is co-financed by Greece and the European Union (European Social Fund-ESF) through the Operational Programme 'Human Resources Development, Education and Lifelong Learning 2014-2020' in the context of the project 'On the interaction of Type Ia Supernovae with Planetary Nebulae' (MIS 5049922). AC is grateful to Noam Soker for many helpful discussions on the topic of jets interaction with supernova remnants. In addition, we thank Rony Keppens for providing us with the AMRVAC code. AC acknowledge the support of this work by the project 'PROTEAS II' (MIS 5002515),which is implemented under the Action 'Reinforcement of the Research and Innovation Infrastructure', funded by the Operational Programme 'Competitiveness, Entrepreneur-ship and Innovation' (NSRF 2014-2020) and co-financed by Greece and the European Union (European Regional Development Fund). The Aristarchos telescope is operated at Helmos Observatory by the IAASARS of the National Observatory of Athens.

DATA AVAILABILITY

The data underlying this article will be shared on reasonable request to the corresponding author.

REFERENCES

Badenes C., Borkowski K. J., Hughes J. P., Hwang U., Bravo E., 2006, ApJ, 645, 1373
Bartel N. et al., 1987, ApJ, 323, 505
Bear E., Grichener A., Soker N., 2017, MNRAS, 472, 1770
Bjorkman J. E., Cassinelli J. P., 1993, ApJ, 409, 429
Blondin J. M., Lundqvist P., Chevalier R. A., 1996, ApJ, 472, 257
Borkowski K. J., Reynolds S. P., Hwang U., Green D. A., Petre R., Krishnamurthy K., Willett R., 2013, ApJ, 771, L9
Borkowski K. J., Gwynne P., Reynolds S. P., Green D. A., Hwang U., Petre R., Willett R., 2017, ApJ, 837, L7
Brandner W., Grebel E. K., Chu Y.-H., Weis K., 1997, ApJ, 475, L45
Burkey M. T., Reynolds S. P., Borkowski K. J., Blondin J. M., 2013, ApJ, 764, 63
Castelletti G., Dubner G., Golap K., Goss W. M., 2006, A&A, 459, 535
Chevalier R. A., 1982a, ApJ, 258, 790
Chevalier R. A., 1982b, ApJ, 259, 302
sChevalier R. A., Blondin J. M., Emmering R. T., 1992, ApJ, 392, 118
Chiotellis A., Schure K. M., Vink J., 2012, A&A, 537, A139
Chiotellis A., Boumis P., Spetsieri Z. T., 2020, Galaxies, 8, 38
Chugai N. N., 2001, MNRAS, 326, 1448
Cikota A., Patat F., Cikota S., Spyromilio J., Rau G., 2017, MNRAS, 471, 2111
Clark D. M., López J. A., Edwards M. L., Winge C., 2014, AJ, 148, 98
Clyne N., Akras S., Steffen W., Redman M. P., Gonçalves D. R., Harvey E., 2015, A&A, 582, A60
Crotts A. P., Heathcote S. R., 1991, Nature, 350, 683
Decin L. et al., 2020, Science, 369, 1497
Drew J. E. et al., 2005, MNRAS, 362, 753
Dwarkadas V. V., Chevalier R. A., 1998, ApJ, 497, 807
Ellison D. C., Decourchelle A., Ballet J., 2004, A&A, 413, 189
Fabrika S., 2004, Astrophys. Space Phys. Rev., 12, 1
Frew D. J., Parker Q. A., Bojičić I. S., 2016, MNRAS, 455, 1459
Gaensler B. M., Green A. J., Manchester R. N., 1998, MNRAS, 299, 812
García-Segura G., Langer N., Różyczka M., Franco J., 1999, ApJ, 517, 767
Grichener A., Soker N., 2017, MNRAS, 468, 1226
Hamuy M. et al., 2003, Nature, 424, 651
Heger A., Langer N., Woosley S. E., 2000, ApJ, 528, 368
Hillebrandt W., Hoeflich P., Weiss A., Truran J. W., 1987, Nature, 327, 597
Huggins P. J., Mauron N., Wirth E. A., 2009, MNRAS, 396, 1805
Igumenshchev I. V., Tutukov A. V., Shustov B. M., 1992, SvA, 36, 241
Katsuda S. et al., 2016, ApJ, 832, 194
Keppens R., Nool M., Tóth G., Goedbloed J. P., 2003, Computer Physics Communications, 153, 317
Kramer M., Lyne A. G., Hobbs G., Löhmer O., Carr P., Jordan C., Wolszczan A., 2003, ApJ, 593, L31
Livio M., Mazzali P., 2018, Phys. Rep., 736, 1
Mastrodemos N., Morris M., 1999, ApJ, 523, 357
Matt S., Balick B., 2004, ApJ, 615, 921
Mauerhan J. et al., 2014, MNRAS, 442, 1166
Meaburn J., 1987, MNRAS, 229, 457
Millas D., Porth O., Keppens R., 2019, in Sauty C., ed., Astrophysics and Space Science Proceedings Vol. 55, JET Simulations, Experiments, and Theory: Ten Years After JETSET. What Is Next?. Springer, Berlin, p. 71
O'Connor J. A., Redman M. P., Holloway A. J., Bryce M., López J. A., Meaburn J., 2000, ApJ, 531, 336
Orlando S. et al., 2020, A&A, 636, A22
Plait P. C., Lundqvist P., Chevalier R. A., Kirshner R. P., 1995, ApJ, 439, 730
Politano M., Taam R. E., 2011, ApJ, 741, 5
Reilly E., Maund J. R., Baade D., Wheeler J. C., Höflich P., Spyromilio J., Patat F., Wang L., 2017, MNRAS, 470, 1491
Reynolds S. P., Borkowski K. J., Hwang U., Hughes J. P., Badenes C., Laming J. M., Blondin J. M., 2007, ApJ, 668, L135
Santander-García M., Rodríguez-Gil P., Corradi R. L. M., Jones D., Miszalski B., Boffin H. M. J., Rubio-Díez M. M., Kotze M. M., 2015, Nature, 519, 63
Schure K. M., Kosenko D., Kaastra J. S., Keppens R., Vink J., 2009, A&A, 508, 751
Smith N., 2002, MNRAS, 337, 1252
Smith N., 2007, AJ, 133, 1034
Smith N., Arnett W. D., 2014, ApJ, 785, 82
Smith N., Bally J., Walawender J., 2007, AJ, 134, 846
Soker N., 2019, New Astron. Rev., 87, 101535
Tiffany C., Humphreys R. M., Jones T. J., Davidson K., 2010, AJ, 140, 339
Townsend R. H. D., Owocki S. P., 2005, MNRAS, 357, 251
Truelove J. K., McKee C. F., 1999, ApJS, 120, 299
Tsebrenko D., Soker N., 2013, MNRAS, 435, 320
Tsebrenko D., Soker N., 2015a, MNRAS, 447, 2568
Tsebrenko D., Soker N., 2015b, MNRAS, 450, 1399
Tsebrenko D., Soker N., 2015c, MNRAS, 453, 166
Vink J., 2008, ApJ, 689, 231
Warren D. C., Blondin J. M., 2013, MNRAS, 429, 3099
Warren J. S., Hughes J. P., Slane P. O., 2003, ApJ, 583, 260
Weaver R., McCray R., Castor J., Shapiro P., Moore R., 1977, ApJ, 218, 377
West R. M., Lauberts A., Jorgensen H. E., Schuster H. E., 1987, A&A, 177, L1
Williams B. J., Borkowski K. J., Reynolds S. P., Ghavamian P., Blair W. P., Long K. S., Sankrit R., 2012, ApJ, 755, 3
Yu H., Fang J., 2018, Res. Astron. Astrophys., 18, 117

This paper has been typeset from a TEX/LATEX file prepared by the author.